Time-lapse attenuation-attribute variations during CO_2 injection using DAS VSP data from the CaMI.FRS

Yichuan Wang and Don Lawton

ABSTRACT

For seismic monitoring injected CO_2 during geologic CO_2 storage, it is useful to measure time-lapse (TL) variations of seismic attenuation. Seismic attenuation directly connects to different petrophysical parameters of the CO_2 storage complex. We have developed an approach to derive smooth time-variant spectra from seismic signal by using sparse strongest signal peaks, and then measure two different attributes characterizing the path effects of seismic attenuation from the smooth spectra. This approach is straightforward and does not require sophisticated algorithm or parameterization scheme. We apply this approach to TL DAS VSP data from the Field Research Station (FRS) CO_2 injection project in southern Alberta, Canada. High-quality stacked reflection records are obtained from baseline and monitor DAS VSP surveys at the FRS and TL attenuation-attribute differences are derived from these reflection records. TL variations of attenuation attributes are observed within the injection zone at the FRS, which are interpreted as being related to the injected CO_2. Although there is always a significant trade-off between the accuracy and temporal resolution of the measured attenuation parameters, reliable attenuation measurements around the injection zone are still achieved with in-use reflection signal of a sufficient length and bandwidth. Attenuation attributes measured from this approach can be an advantageous tool for monitoring the distribution and migration of CO_2 plumes, especially for TL monitoring with DAS data that is with high noise level or with apparent acquisition or noise difference between different vintages.

INTRODUCTION

Time-lapse (TL) seismic methods (Lumley, 2001) are used to monitor the distribution of CO_2 plumes within the injection zone and determining if CO_2 leakage is occurring above the storage zone. Compared with TL surface seismic data, TL vertical seismic profile (VSP) is more cost-effective and provides higher resolution and repeatability near the wellbore. These benefits make VSP an effective alternative to surface seismic surveys for monitoring injected CO_2, especially during early stages of an injection program when the CO_2 plume is still close to the injection well. For commercial, pilot, or demonstration CO_2 storage projects, TL VSPs have been acquired with conventional geophones or distributed acoustic sensing (DAS) fiber cable. The rapid development of DAS technology promotes its use in borehole VSP for monitoring, with the advantages such as long-term deployment, low installation cost, large vertical coverage at small spatial sampling, and concurrent data acquisition and CO_2 injection.

Multiple DAS VSP surveys have been acquired for the present study at the Field Research Station (FRS) in Alberta, Canada (Figure 1; Macquet et al., 2022), developed by the Containment and Monitoring Institute (CaMI) of Carbon Management Canada. The CO_2 injection project at the CaMI FRS focuses on the development of subsurface and surface measurement, monitoring, and verification (MMV) technologies for CO_2 storage. TL DAS VSP is one of the key technologies being studied and verified at the FRS. As DAS fiber is principally sensitive to longitudinal strain, the deployment of DAS fiber cable in vertical wells is ideal for P-wave VSP surveys to measure physical property changes within the FRS storage complex. For example, the most common velocity change that is normally analyzed through the estimated time shift. However, the injection zone at the FRS is thin and injected CO_2 may cause only a few percent of P-wave velocity decrease that is near the seismic noise level for detection. In addition, the signal-to-noise ratio of VSP data obtained through DAS technology is generally lower than that obtained from geophones. Therefore, some additional physical property, such as seismic attenuation, is important to be explored. Compared with velocity or density variations due to CO_2 injection, attenuation is more sensitive to changes in saturation, permeability, and pore fluid. Estimating TL attenuation-attribute variations from reflection signal of DAS VSP data for monitoring injected CO_2 is presented in this report.

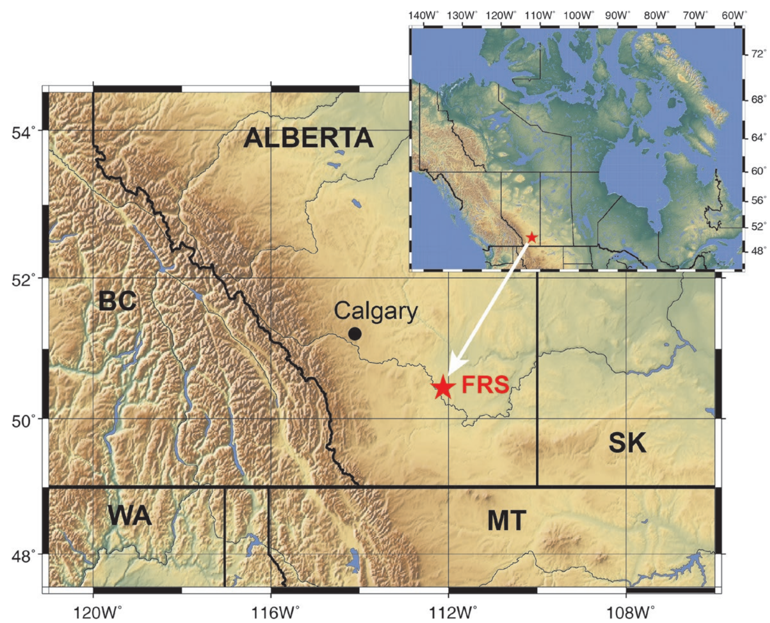

Figure 1: Location map of the CaMI FRS in southern Alberta, Canada.

When measured from reflection seismic data, the attenuation is always "apparent" and closely related to variations of stratigraphic properties. Additionally, the path effect of seismic attenuation should be characterized by not only the traditional inverse quality factor Q^{-1} but also another parameter γ responsible for frequency-independent ("geometric") attenuation (Morozov, 2008, 2011). We measure attenuation parameters Q^{-1} and γ by applying Wang and Morozov's (2020a) approach. The interpretation of measured results helps in characterizing the distribution and migration of the CO_2 plume.

DAS VSP survey and data processing

At the CaMI FRS, since the first CO_2 injection in 2017, a small volume of CO_2 of up to 20 tonnes per year have been injected into a shallow formation at the depth of 300 m. This target formation is the 7 m Basal Belly River Sandstone (BBRS). There is one CO_2 injection well and two 350 m deep observation wells (OBS1 and OBS2, Figure 2) at the FRS. In addition, there is a southwest–northeast (SW–NE) oriented horizontal trench centered close to OBS2. DAS fiber cables with a continuous loop in the horizontal trench and in the two observation wells are permanently installed. The fiber cables are from the top to the maximum depth of 348 m in OBS1 and 334 m in OBS2. Several DAS VSP surveys have been acquired at the FRS, and the surveys analyzed in this report include the baseline one acquired in May 2017 and the monitor one acquired in March 2021. Figure 2 shows the shot locations of one walk-around and three walk-away lines of this monitor survey. This study measures the attenuation attributes for walk-away VSP data acquired along Line 13 and Line 15. The baseline DAS VSP survey before any CO_2 injection was acquired in May 2017 for Line 13, but not acquired for Line 15. The seismic acquisition repeatability for Line 13 is very good due to the permanent installation of DAS fiber cables and the same source type.

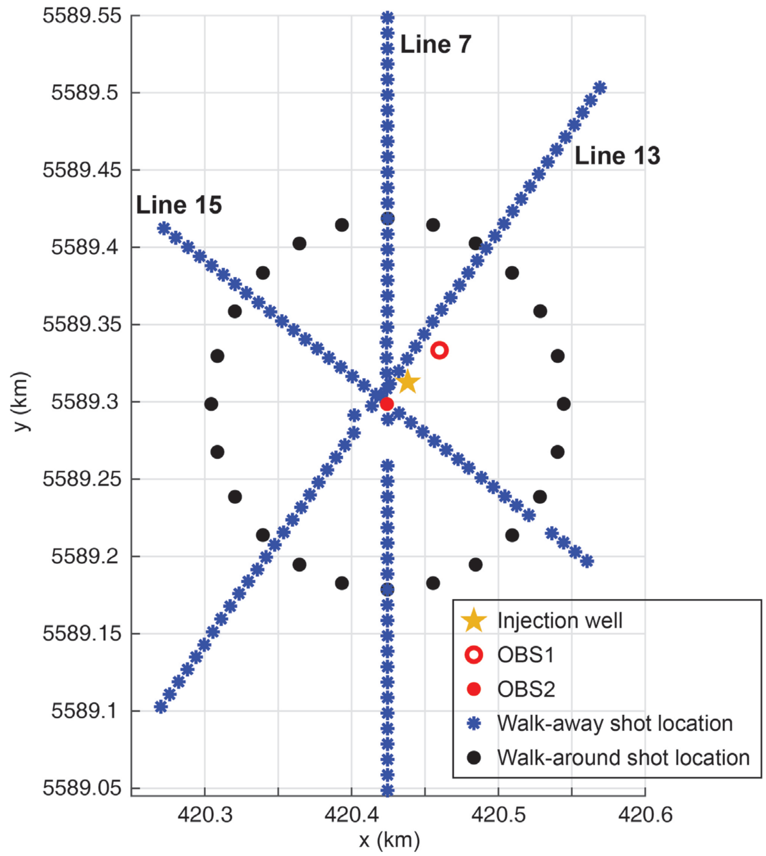

Figure 2: VSP layout map of the survey acquired in March 2021.

We apply identical data processing for the different vintages of DAS data. As we construct attenuation-attribute images from reflection signal for monitoring the injected CO_2, upgoing P-wave reflections must be isolated from DAS VSP data. We separate downgoing and upgoing wavefields through the application of a 29-point median filter followed by a frequency-wavenumber (f-k) filter. Figure 3a shows the sum of data from downward and upward straight fiber in OBS2, in which downgoing P- or S-wave energy and upgoing P-wave energy are visible. After the median filter (Figure 3b) and f-k filter (Figure 3c), the upgoing P-wave reflections are clearly isolated and evident over the entire depth coverage of the fiber. Stacked seismic records can then be obtained from the isolated upgoing reflections after other standard VSP processing steps such as deconvolution, bandpass filtering, normal moveout correction and CDP stacking.

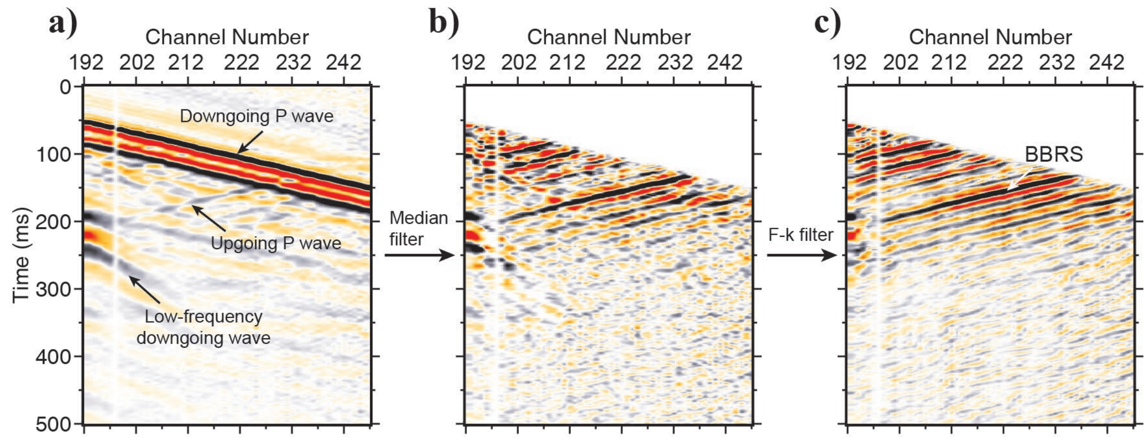

Figure 3: Wavefield separation: (a) the sum of raw DAS data from downward and upward straight fiber in OBS2, and isolated upgoing wavefield after (b) median filter and then (c) f-k filter. BBRS reflection is indicated in plot (c).

TIME-LAPSE ATTENUATION MEASUREMENTS

Seismic attenuation is typically estimated in frequency domain. The key requirement for different frequency-domain methods is the accurate determination of amplitude spectra. In this study, time-variant spectra are calculated by applying Wang and Morozov's (2020a) approach of iterative identifying locally strongest reflection peaks and stacking their waveforms. We then estimate attenuation parameters (Q^{-1} and γ) from the time-variant spectra as the coefficients of linear regression with respect to frequency, and derive their TL differences for monitoring the injected CO_2 at the FRS. As the accuracy of estimated attenuation parameters can be limited and trades off with the temporal resolution (White, 1992), we also evaluate the attainable accuracy and resolution for the measured results at the FRS.

Seismic attenuation model and measurement

In frequency domain, the non-stationary convolutional model for seismic reflection signal is

$$A(t,f) = S(f)R(t,f)F(t,f)G(t) \tag{1}$$

where t is the two-way reflection time, f is the frequency, $A(t,f)$ is the time-frequency variant amplitude of the reflection signal, $S(f)$ is the spectrum of the seismic source, $R(t,f)$ is the time-frequency response of the reflectivity, and $F(t,f)$ and $G(t)$ are the path effects on the signal spectra. The anelastic path factor $F(t, f)$ is associated with seismic attenuation and related to the traditional factor Q of the medium as $F(t,f) = \exp\left[-\pi f \int_0^t Q^{-1}(\tau)\,d\tau\right]$. The elastic path factor $G(t)$ is associated with focusing or defocusing and exponentially varies as $G(t)=\exp\left[-\int_0^t \gamma(\tau)\,d\tau\right]$, where γ is a "geometric" counterpart for Q^{-1} (Morozov, 2008).

Taking the logarithm and then the time derivative of equation 1 gives

$$\frac{\partial}{\partial t}\left[\ln R(t,f)-\ln A(t,f)\right]=\gamma+\pi f Q^{-1}. \tag{2}$$

Due to the fundamental difficulty that $F(t,f)$ and $R(t,f)$ in equation 1 cannot be differentiated in seismic reflection signal, $\gamma(t)$ and $Q^{-1}(t)$ are inverted for with the assumption of "white" reflectivity (Robinson, 1957; $R(t,f) = const$):

$$-\frac{\partial \ln A(t,f)}{\partial t}=\gamma_A+\pi f Q_A^{-1}. \tag{3}$$

In relation 3, γ_A and Q_A^{-1} are the *apparent* attenuation parameters and obtained as the coefficients of linear regression with respect to frequency f. The evaluation of γ_A and Q_A^{-1} requires smooth estimates of time-variant spectra $A(t,f)$.

We use Wang and Morozov's (2020a) approach to derive the smooth estimates of $A(t,f)$ as follows. Considering a reflected signal $u(t)$, we first identify within it a sparse set of strongest peaks at times t_j, where j is the number of selected peaks. Time intervals between the identified peaks at t_j are selected to exceed a certain threshold for keeping the sparsity. For each peak j, we extract a waveform $w_j(\tau)$ of length T_w centered at the peak. Then, centered on any time t_i, we extract a segment i of length T from $u(t)$ and stack all waveforms $w_j(\tau)$ located within this segment to produce the estimated signal waveform (Wang and Morozov, 2020a):

$$s(t_i,\tau)=c\sum_{j\in\text{segment } i}\frac{h\left[\left(t_j-t_i\right)/T\right]}{w_j(0)}w_j(\tau), \tag{4}$$

where c is the factor that scales the peak amplitude to $s(t_i,0) = 1$. The Hann time window h in equation 4 is of the same length T with segment i and applies weights to $w_j(\tau)$ located within different parts of the segment i. Therefore, the waveform $s(t_i,\tau)$ at time t_i and its spectrum $S(t_i,f)$ are insensitive to segment edges. The temporal resolution of the resulting spectra can be estimated as the half segment length $T/2$.

The amplitude variation within the signal $u(t)$ is distorted by the scaling procedure in equation 4. To restore this amplitude, we normalize the spectrum $S(t_i,f)$ from equation 4 so that the root-mean-square (RMS) amplitude of the normalized spectrum $\overline{S}(t_i,f)$ equals one, and then measure the RMS amplitude of each segment i from $u(t)$, denoted as

$u_i^{\mathrm{rms}}\left(t_i\right)$. The time-variant spectra for attenuation measurements from equation 3 are finally calculated as

$$A\left(t_i, f\right) = u_i^{\mathrm{rms}}\left(t_i\right)\overline{S}\left(t_i, f\right). \tag{5}$$

The $A(t_i, f)$ from equation 5 would preserve the amplitude and spectral variations of the signal, and be smooth in time t_i due to the use of Hann function in equation 4.

Time-lapse attenuation-attribute variations

The described approach of the preceding subsection is first applied to monitor VSP CDP stacks from walk-away Line 13 and Line 15 acquired in March 2021 (Figure 2). There had been approximately 34 tonnes of CO_2 injected at the FRS prior to this acquisition date. Figure 4 shows the measured apparent attenuation parameters γ_A and Q_A^{-1} (equation 3) from the monitor VSP CDP stacks. For the measurements from both Line 13 (Figure 4a to 4c) and Line 15 (Figure 4d to 4f), there are large positive Q_A^{-1} and large negative γ_A (focusing) around OBS2 at the BBRS injection zone. Along Line 13 at the BBRS depth, the Q_A^{-1} and γ_A decrease from approximately 0.08 and –14 s^{-1} on the SW of OBS2 to approximately 0.06 and –10 s^{-1} on the NE of OBS2, respectively. These values are consistent with the measurements from Line 15, where the Q_A^{-1} and γ_A are approximately 0.07 and –12 s^{-1} at the location of OBS. The large Q_A^{-1} and γ_A are interpreted to be related to increased CO_2 saturation and/or pore pressure, and the consistency of estimated Q_A^{-1} or γ_A values around OBS2 from two different lines indicates that the described approach can obtain stable attenuation-attribute measurement from field data such as DAS VSP.

The baseline walkaway VSP survey prior to any CO_2 injection had been acquired in May 2017 for Line 13 only. Figure 5 shows the estimated γ_A and Q_A^{-1} from the baseline VSP CDP stack and the TL responses (monitor minus baseline) along Line 13. Due to a slight difference in the number of shots, the length of Line 13 from the baseline survey is shorter than that from monitor survey. Nevertheless, identical CDP grids were used for the two vintages. In Figure 5, the measurements from baseline data show there is no attenuation anomaly at the BBRS target zone prior to CO_2 injection, but the TL responses show a clear increase in attenuation to the southwestern of OBS2 at the BBRS depth. This attenuation increase is not seen around the injection well and we interpret it as indicating the migration of the injected CO_2 (e.g., along the directions of maximum horizontal stress), which changes from liquid phase at the injection well to gas phase at the leading edge of the plume.

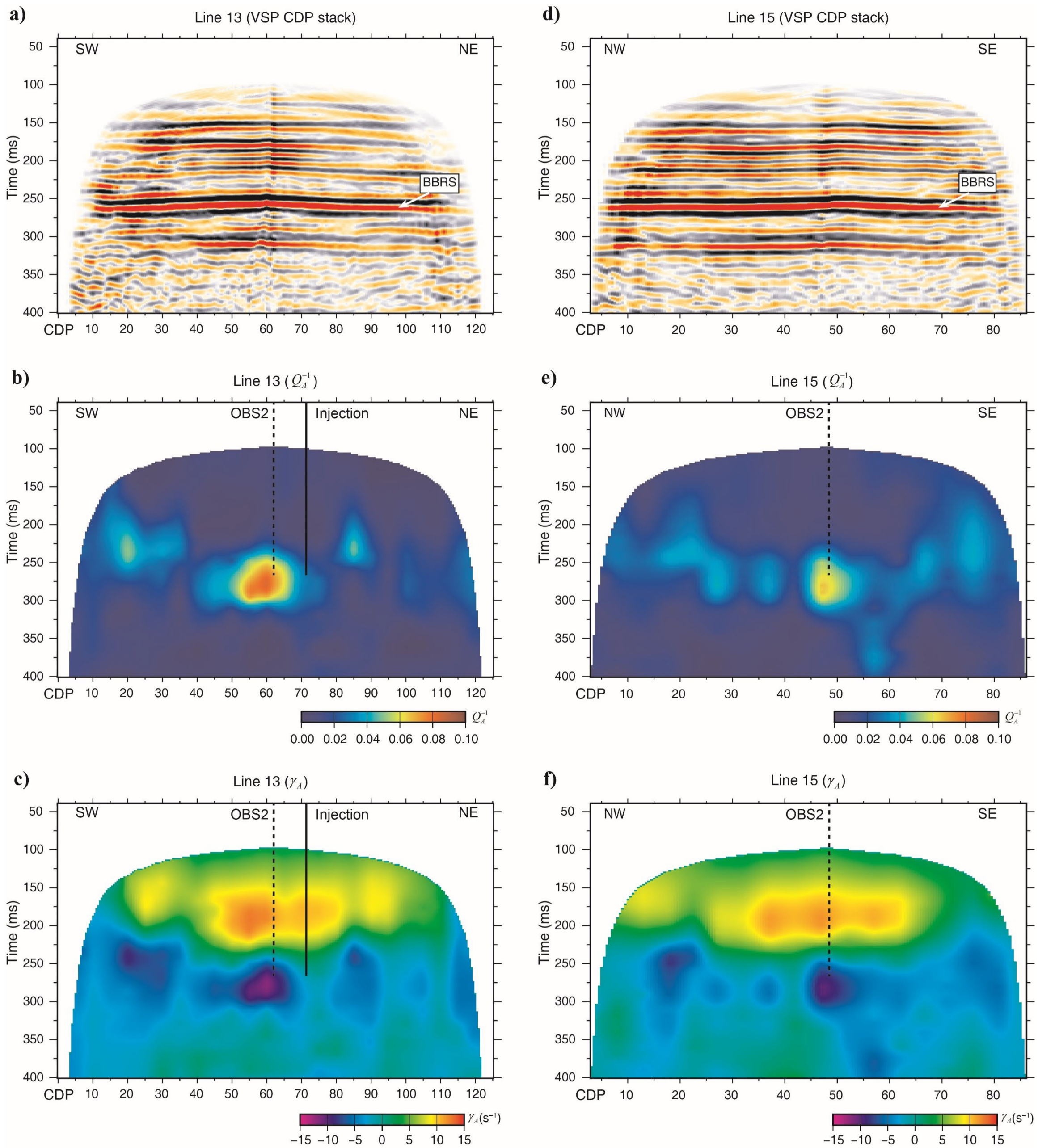

Figure 4: Attenuation-attribute measurements from monitor data along (a-c) SW–NE Line 13 and (d-e) NW–SE Line 15: (a and d) monitor VSP CDP stack with BBRS reflection indicated, (b and e) estimated Q_A^{-1}, and (c and f) estimated γ_A. Dashed and solid black lines indicate OBS2 and injection well (labeled), respectively.

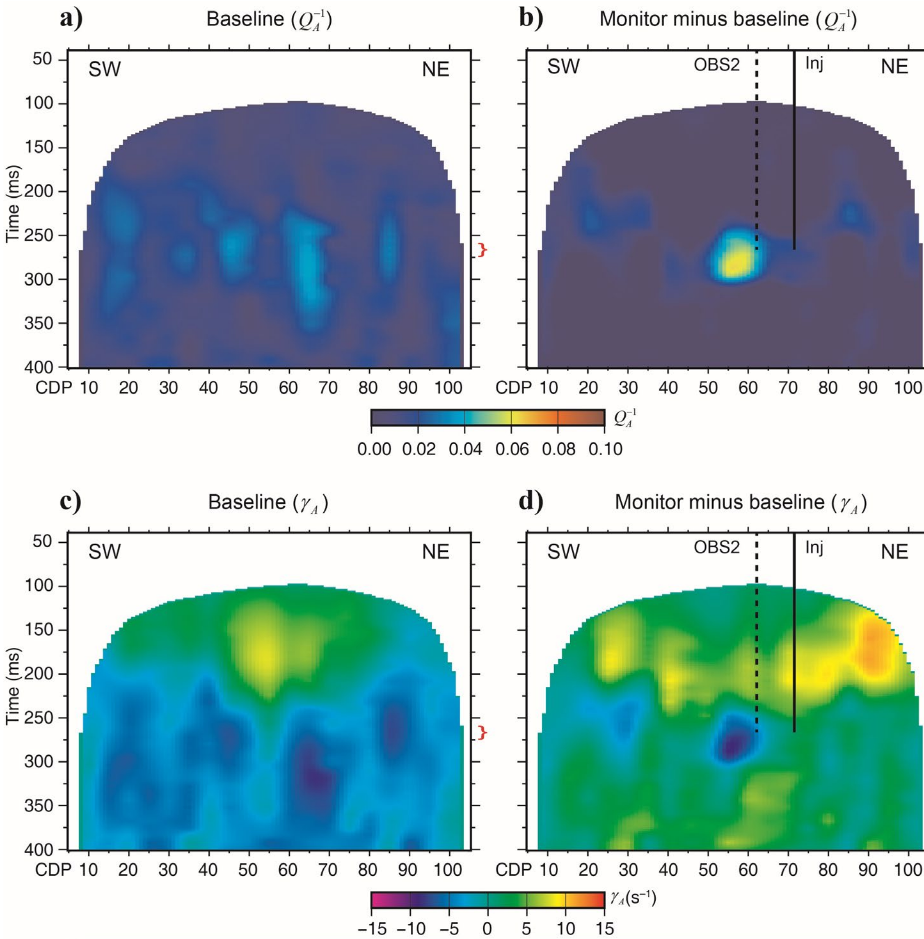

Figure 5: TL attenuation-attribute variations along SW–NE Line 13: (a) estimated Q_A^{-1} from baseline VSP CDP stack, (b) TL Q_A^{-1} variation, (c) estimated γ_A from baseline VSP CDP stack, and (d) TL γ_A variation. Red bracket indicates BBRS injection zone.

Accuracy and resolution of estimated attenuation

Although the attenuation measurements in this report are from high-quality DAS VSP data, the finite extent and limited sampling in the time-frequency plane can still cause strong limitations on the accuracy of measured Q^{-1} and γ. The errors of measured Q^{-1} and γ can thus be significant and trade off with the temporal resolution (White, 1992). Therefore, it is important to quantitatively evaluate if the measured Q^{-1} and γ are stable and accurate for detecting subtle in situ changes between the TL data. Based on the model by White (1992) and recently by Wang and Lawton (2022), we estimated the errors and temporal resolution limit for the measurement results shown in the preceding subsection.

To obtain uncorrelated estimates of Q^{-1} and γ, it is convenient to evaluate linear regression with respect to a demeaned variable $\left(f_m - \bar{f}\right)$ as

$$a_m = \gamma + \pi\left(f_m - \bar{f}\right)Q^{-1}, \tag{6}$$

where a is the spectral quantity in the left-hand side of equation 3, and $\overline{f}$ is the mean value of frequencies f_m. Denoting B the available frequency bandwidth of the data and b the elementary frequency bandwidth, Q^{-1} and γ are estimated by regression 6 with $N = B/b$ frequencies f_m. Note that T_w is the length of waveform ($w_j(\tau)$ in equation 4) in spectral measurement. The minimum value of b for containing mutually independent spectral components would be $b = 1/2T_w$.

As Q^{-1} and γ are normally distributed, standard statistical methods could be used to evaluate their measurement accuracy. The measurement errors (i.e., square root of variance) of estimated coefficients $\hat{\gamma}$ and $\hat{Q}^{-1}$ from regression 6 are thus

$$s_{\hat{\gamma}} = \frac{\sigma_{\hat{a}}}{\sqrt{N}} \text{ and } s_{\hat{Q}^{-1}} = \frac{\sigma_{\hat{a}}}{\pi\sqrt{\sum\left(f_m - \overline{f}\right)^2}} = \frac{s_{\hat{\gamma}}}{\pi\left\langle f_m - \overline{f}\right\rangle_{RMS}}, \tag{7}$$

where $\sigma_{\hat{a}}^2$ is the variance of the estimated spectral quantity $\hat{a}$, and $\left\langle f_m - \overline{f}\right\rangle_{RMS}$ denotes the RMS average of demeaned frequencies which is proportional to the bandwidth of the data as $\left\langle f_m - \overline{f}\right\rangle_{RMS} = c_0 B$. The spectral quantity a ($-\partial \ln A(t,f)/\partial t$ in equation 3) can be approximated as the ratio of amplitude spectra at times t_p and t_q:

$$a_m \approx \frac{\ln\left[A\left(t_p, f_m\right)/A\left(t_q, f_m\right)\right]}{\Delta t}, \tag{8}$$

where $\Delta t = t_q - t_p$. If the interval Δt is sufficiently large, the two spectra would be statistically uncorrelated and the relative variance of the spectral ratio is (White, 1992)

$$\frac{\operatorname{var}\left\{\left|A\left(t_p, f_m\right)/A\left(t_q, f_m\right)\right|\right\}}{\left|A\left(t_p, f_m\right)/A\left(t_q, f_m\right)\right|^2} = \operatorname{var}\left\{\ln\left|A\left(t_p, f_m\right)/A\left(t_q, f_m\right)\right|\right\} = \frac{1}{2bT_w}. \tag{9}$$

By using equations 8 and 9, equations 7 become (Wang and Lawton, 2022)

$$s_{\hat{\gamma}} = \frac{1}{\sqrt{2}\Delta t}\frac{1}{\sqrt{BT_w}} \text{ and } s_{\hat{Q}^{-1}} = \frac{s_{\hat{\gamma}}}{\pi c_0 B} = \frac{1}{\pi\sqrt{2}c_0\Delta t}\frac{1}{\sqrt{B^3 T_w}}. \tag{10}$$

From equations 10, the errors $s_{\hat{\gamma}}$ and $s_{\hat{Q}^{-1}}$ are independent of $\hat{\gamma}$ and $\hat{Q}^{-1}$ magnitude and the key parameter for determining the measurement accuracy is the temporal resolution Δt.

In this study, the temporal resolution Δt is measured as half length of the segment i in equation 4 for spectral measurements. The length of segment i is T = 400 ms for the measurements (Figure 4 and Figure 5) in the preceding subsection. Figure 6 shows the time-variant seismic spectra $A(t_i, f)$ (equation 5) from the trace of CDP number 51 (close to OBS2) in Figure 4d, the estimated $\hat{\gamma}$ and $\hat{Q}^{-1}$, and their empirical (equations 7) and theoretical (equations 10) errors by using $\Delta t = T/2 = 200$ ms. The $A(t_i, f)$ in Figure 6b are smooth as required for the estimations of Q^{-1} and γ from regression 3. The two errors (red and green lines) in Figure 6c or 6d are close and the theoretical ones from equations 10 are $s_{\hat{\gamma}} \approx 1.86$ and $s_{\hat{Q}^{-1}} \approx 0.023$. The estimated $\hat{Q}^{-1}$ for most depths above and below the BBRS in Figure 6c is below the error $s_{\hat{Q}^{-1}} \approx 0.023$, which indicates an limited accuracy of estimated $\hat{Q}^{-1}$ for these areas outside of injection zone. However, around the BBRS that is with high apparent attenuation in Figure 6c, the estimated $\hat{Q}^{-1}$ values are much larger than the $s_{\hat{Q}^{-1}} \approx 0.023$. Meanwhile, the accuracy of estimated $\hat{\gamma}$ is higher with the theoretical error $s_{\hat{\gamma}} \approx 1.86$ smaller than the $\hat{\gamma}$ values for all the depths in Figure 6d. In summary, under the limited resolution of $\Delta t = 200$ ms, the measured attenuation attributes around the BBRS that reflect changes due to injected CO_2 are considered reliable.

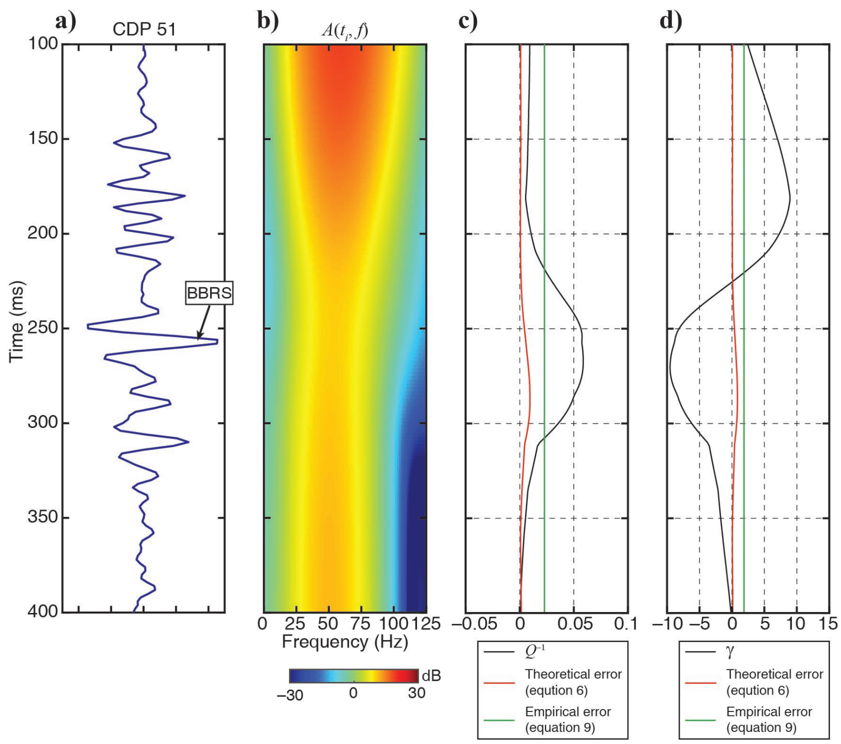

Figure 6: Measurement errors of estimated attenuation parameters: (a) stacked trace of CDP number 51 in Figure 4d with BBRS reflection indicated, (b) time-variant spectra from the trace in plot (a) (equation 5), estimated (c) Q^{-1} and (d) γ and their measurement errors (legend).

Figure 7 shows the dependencies of the relative uncertainties of the frequency-dependent attenuation $e_{\hat{q}} = s_{\hat{q}} / \hat{q}$ and geometric attenuation $e_{\hat{\gamma}} = s_{\hat{\gamma}} / |\hat{\gamma}|$ (equations 10) on the temporal resolution of the spectrogram and the attenuation levels themselves. From Figure 7, we can observe a significant trade-off between the accuracy of estimated $\hat{q}$ or $\hat{\gamma}$ and the temporal resolution Δt. For $\Delta t = 200$ ms (the black dashed lines in Figure 7) used in this study, the estimated $\hat{q}$ needs to be larger than ~0.09 and the estimated $|\hat{\gamma}|$ needs to be larger than ~6.5 s^{-1} for achieving an error lower than 30%. For the typical large value of $\hat{q} = 0.08$ and $|\hat{\gamma}| = 10$ s^{-1} (the black solid lines in Figure 7) around the BBRS injection zone, the relative errors under Δt = 200 ms are modest $e_{\hat{q}} \approx 34\%$ and $e_{\hat{\gamma}} \approx 20\%$. However, for the non-injection zones with much smaller $\hat{q}$ and $\hat{\gamma}$, the relative errors are prohibitively large even with much lower resolution.

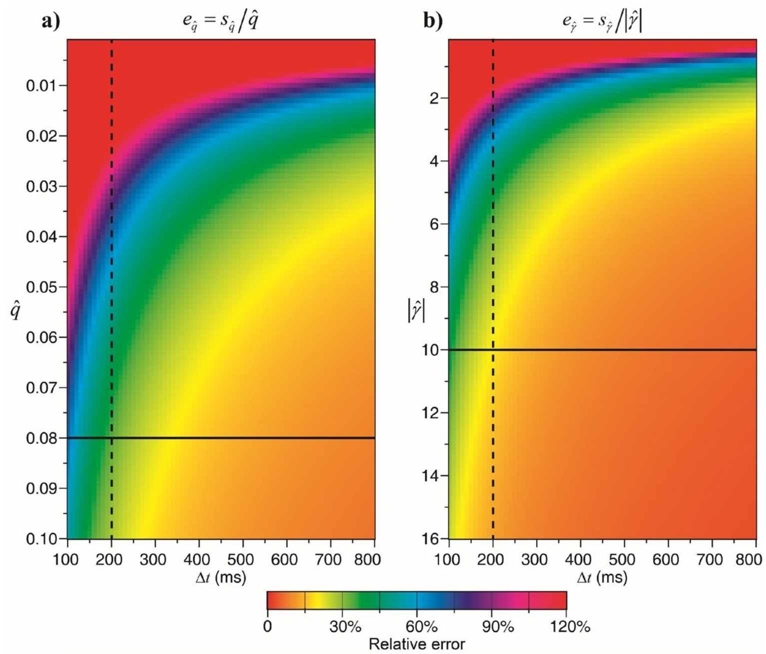

Figure 7: Relative errors of estimated (a) $\hat{q}$ and (b) $\hat{\gamma}$ with different temporal resolution Δt and $\hat{q}$ or $|\hat{\gamma}|$ values. Dashed black lines indicate the value $\Delta t = 200$ ms used in this study. Solid black lines in (a) and (b) show the levels $\hat{q} = 0.08$ and $|\hat{\gamma}| = 10$ s^{-1}, respectively.

DISCUSSION

As attenuation is sensitive to changes in saturation, permeability, and pore fluid, the estimated TL attenuation difference (Figure 5) can likely be a standard tool for detecting subtle in situ changes within the subsurface. In addition, velocity is one of the most common physical properties explored during TL seismic monitoring. In this section, we analyze velocity variations through the estimation of time shifts. We aim to investigate if there is any correlation of the estimated time shifts with the attenuation-attribute variations measured in the preceding section.

We apply Wang and Morozov's (2020b) TL waveform calibration to obtain time shifts. This approach matches each stacked monitor trace to the corresponding baseline trace by three operations of time shifting, amplitude correction, and spectral shaping. The time shifts between baseline and monitor reflections are measured during the time shifting of the calibration procedure. Ideally, if no CO_2 leakage is occurring, there should be no time shifts for the shallow layers that are above the BBRS injection zone. In Figure 8, we then subtract the time shifts along a strong reflection horizon (~180 ms in depth) earlier than the BBRS reflection from the time shifts along the first horizon right after the BBRS reflection. There are large negative time shifts of approximately 0.5 ms around CDP number 60 in Figure 8, which is to the southwestern side of OBS2, corresponding well to the distribution of attenuation-attribute variations as shown in Figure 5 and interpreted as being related to the gas-phase CO_2. Note that some time shifts shown in Figure 8 are positive, which are challenging to be interpreted but may be due to unresolved surface statics, noise-related instability or pressure changes from the CO_2 injection.

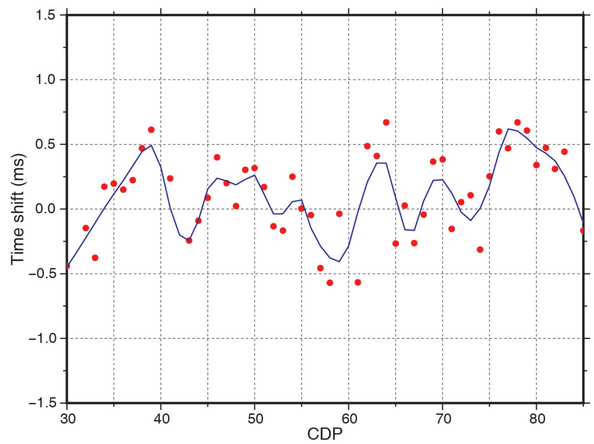

Figure 8: Traveltime changes along the first reflection horizon below the BBRS by subtracting time shifts along a shallow horizon. Blue line is a smooth line through locally weighted scatterplot smoothing.

CONCLUSION

For a CO_2 injection project at the CaMI FRS in Alberta, Canada, multiple DAS VSP surveys have been acquired for TL monitoring. After upgoing wavefield separation, stacked reflection records are obtained and TL variations of attenuation attributes (both Q^{-1} and its "geometric" counterpart γ) are measured from VSP CDP stacks. By deriving smooth time-variant spectra from a sparse set of locally strongest reflection peaks, Q^{-1} and γ are measured as the coefficients of linear regression with respect to frequency. The variations of attenuation attributes are correlated with injection zone and interpretated as caused by increased CO_2 saturation. Evaluations of measurement accuracy also show the measured Q^{-1} and γ of large values around the injection zone are reliable. Such attenuation attributes can be advantageous to geologic CO_2-storage monitoring. The measured time shifts between the monitor and baseline surveys show some correlation with the attenuation-attribute results but require further work. The comparison also demonstrates that for inverting from DAS VSP data attenuation is perhaps a more sensitive property than velocity for monitoring injected CO_2 at the FRS.

ACKNOWLEDGEMENTS

We thank the sponsors of CREWES for continued support. This work was funded by CREWES industrial sponsors and NSERC (Natural Science and Engineering Research Council of Canada) through the grant CRDPJ 543578-19. The data were acquired through a collaboration with Containment and Monitoring Institute (CaMI) of Carbon Management

Canada (CMC). Research at the CMC field site is supported in part by the Canada First Research Excellence Fund, through the Global Research Initiative at the University of Calgary and the CMC Joint Industry Project. The first author is also supported by Canada First Research Excellence Fund, through the Global Research Initiative at the University of Calgary.

REFERENCES

Lumley, D. E., 2001, Time-lapse seismic reservoir monitoring: Geophysics, 66, 50–53, doi: 10.1190/1.1444921.

Macquet, M., D. Lawton, K. Osadetz, G. Maidment, M. Bertram, K. Hall, B. Kolkman-Quinn, J. Monsegny, F. Race, G. Savard, and Y. Wang, 2022, Overview of Carbon Management Canada's pilot-scale CO_2 injection site for developing and testing monitoring technologies for carbon capture and storage, and methane detection: CSEG Recorder, 47, no. 1, 1–27.

Morozov, I. B., 2008, Geometric attenuation, frequency dependence of *Q*, and the absorption band problem: Geophysical Journal International, 175, 239–252, doi: 10.1111/j.1365-246X.2008.03888.x.

Morozov, I. B., 2011, Mechanisms of geometric attenuation: Annals of Geophysics, 54, 235–248, doi: 10.4401/ag-4780.

Wang, Y., and I. B. Morozov, 2020a, A simple approach to nonstationary source waveform estimation in seismic records: Geophysics, 85, no. 3, V257–V268, doi: 10.1190/geo2019-0133.1.

Wang, Y., and I. B. Morozov, 2020b, Time-lapse acoustic impedance variations after CO_2 injection in Weyburn Field: Geophysics, 85, no. 1, M1–M13, doi: 10.1190/geo2019-0221.1.

Wang, Y., and D. C. Lawton, 2022, Time-lapse attenuation variations during CO_2 injection using DAS VSP data from the CaMI Field Research Station, Alberta, Canada: Second International Meeting for Applied Geoscience & Energy, SEG & AAPG, Expanded Abstract, 538-542, doi: 10.1190/image2022-3751282.1.

White, R. E., 1992, Accuracy of estimating *Q* from seismic data: Geophysics, 57, 1508–1511, doi: 10.1190/1.1443218.